Indian Journal of Chemistry
Vol. 53A, February 2014, pp. 152-158

Zinc-doped biphasic calcium phosphate nanopowders synthesized via sol-gel method

Gunawan[a, b], I Sopyan[a, *], Suryanto[a] & A Naqshbandi[a]

[a]Department of Manufacturing and Materials Engineering, Faculty of Engineering
International Islamic University Malaysia, 50728 Kuala Lumpur, Malaysia
Email: sopyan@iium.edu.my

[b]Department of Mechanical Engineering, Faculty of Engineering,
Sriwijaya University, Inderalaya 30662, Indonesia

Received 5 August 2013; revised and accepted 28 January 2014

Zinc-doped biphasic calcium phosphate (BCP) powders have been synthesized via sol-gel method. The dopant concentration ions were adjusted at 1, 2, 3, 5, 10 and 15 mol%. The powders have been calcined at varying temperatures ranging from 500-900 °C and then characterized by XRD, FTIR, TG/DTA, TEM and FESEM data. X-ray diffraction patterns show that the phases present in Zn-doped BCP are hydroxyapatite, β-TCP and parascholzite. FTIR analysis reveal that the separation of three PO_4^{3-} stretching peaks is obscure and OH bending peak at 630 cm^{-1} broaden with an increase in Zn concentration, whereas the PO_4^{3-} band of TCP at 1085 cm^{-1} is sharper at higher calcination temperatures. Morphology analysis show that the size of agglomerates tends to increase with the increasing Zn concentration. These findings indicate that an increase in Zn level doped to the BCP affects the phase composition, crystallization and microstructure of the samples.

Keywords: Doping, Zinc doping, Biphasic calcium phosphate, Calcium phosphate, Sol-gel method

Calcium phosphate (CaP) constitutes the inorganic part of human bones and teeth. It has been widely used for various bone and tooth implants due to its excellent biocompatibility and bioactivity. Calcium phosphate may exist in biphasic, triphasic or multiphasic (polyphasic) combinations. Biphasic calcium phosphate (BCP) ceramics, composed of hydroxyapatite (HA, $Ca_{10}(PO_4)_6(OH)_2$) and β-tricalcium phosphate (β-TCP, $Ca_3(PO_4)_2$), are the most extensively used materials for the preparation of bone implants[1]. The physical properties of BCP bioceramics can be attributed to the fact that HA phase is more stable under physiological conditions and also that β-TCP has faster rate of dissolution. BCP ceramics can enhance growth of bone cells inside the implants owing to its biocompatible, osteoconductive and osteoinductive nature. This characteristic enhances bone repair to a considerable extent[2-4]. In recent studies clinical parameters have established as BCP facilitated successful osteogenic process[5]. Therefore, BCP has been considered to be the most favorable and best substitute for human bone reconstructions.

It has been observed that most of natural apatites in the bone comprise several substituted elements such as cations (Mg^{2+}, Mn^{2+}, Zn^{2+}, Na^{+}, Sr^{2+}) and anions (HPO_4^{2-}or CO_3^{2-})[6-9]. Amongst all these ions, Zn is considered to be one of the most essential metal ions since it is involved in bone formation *in vitro* and *in vivo* and has the potential of promoting tissue regeneration[6,10]. The essential roles of zinc include prevention of bone loss and osteoporosis and stimulation of bone metabolism and growth[11,12]. Zinc also has antimicrobial property which increases with an increase in the amount of zinc[13]. In addition, the dissolution rate of zinc-doped hydroxyapatite is faster than that of pure hydroxyapatite[13].

Several methods have been reported for the synthesis of zinc substituted hydroxyapatite including chemical co-precipitation[14], hydrothermal reaction[15] and sol-gel[4]. Sol-gel method, however, has proved to be more advantageous as it involves low temperatures and the products produced are of high purity[16]. Moreover, the substitution of metal ions into BCP via sol-gel method is a simple way to improve densification and mechanical performance of BCP[17,18]. In the present investigation, Zn-doped BCP nanopowders have been synthesized via sol-gel method followed by characterization of the obtained powder.

Materials and Methods

Synthesis of Zn-free and Zn-doped BCP

For the preparation of Zn-free BCP powders[16], ethylenediaminetetraacetic acid (EDTA, 180 g) (Titriplex II, Merck) was added to 500 mL of ammonia

solution (11% NH_4OH) (B&M Chemical) which was heated to a temperature of 60 °C. EDTA was used as a chelating agent to prevent spontaneous precipitation of calcium ions during the gel formation. The amount of EDTA used in this reaction is considered enough for completely chelating Ca^{2+} and Zn^{2+}. This was followed by the addition 130 g of calcium nitrate tetrahydrate [$Ca(NO_3)_2.4H_2O$] (Systerm), and 40 g of diammonium hydrogen phosphate [$(NH_4)_2.HPO_4$] (Merck) which were used as calcium and phosphorus precursors respectively. Then 42.5 g of urea (Systerm) was consequently added as a gelling agent. The formed mixture was then refluxed at 110 °C for 5–6 h with stirring until a white gel of Zn-free BCP mixture was obtained. The obtained gel was dried at 340 °C for 3 h. Drying was done so as to remove the nitrate ions present in the white gel phase. The resulting black powders were calcined in a high temperature furnace (Protherm, PLF 160/5) at a temperature of 500–900 °C, maintaining a heating rate of 10 °C/min and holding time of 3 h before being cooled to room temperature.

Zn-doped BCP was also synthesized in the same way, i. e., zinc nitrate hexahydrate [$Zn(NO_3)_2.6H_2O$] (Friendemann & Schmidt) was used as the dopant (zinc) precursor and was added together with calcium nitrate tetrahydrate. The dopant was added at molar percentage (mol%) of 1, 2, 3, 5, 7, 10 and 15 mol% with respect to Zn:Ca molar ratio.

Characterization of BCP

The crystal structure of the powders was analysed by XRD (Shimadzu, XLab XRD 6000) using Cu-Kα radiation. Diffraction patterns were recorded over a range of 20–60° with a scan speed of 2°/min. Rietveld refinement analysis was conducted using computer-based program General Structure Analysis System (GSAS). The space group (P63/m, No. 176), cell parameters, atomic positions and the thermal parameters of HA were introduced as the initial structural model. Rietveld refinement was performed in several stages[19]. Initially, the scale-factor and background were refined, followed by refinement of the other parameters, *viz.*, profile parameters, zero shift, asymmetric parameter, cell parameters, preferential orientation, atomic coordinates, thermal parameters and occupancy factors of Ca and Zn. Particle size distribution of the powder samples was analyzed using Nanoparticle Sizer (Malvern Instrument, Zen 1600). Samples were prepared by dissolving 0.5 g of powder in 40 mL distilled water followed by stirring for 24 h. The stirred solution (1 mL) was then diluted in 20 mL distilled water and stirred again for 24 hours in order to obtain a well-dispersed solution.

FTIR was recorded on a Perkin Elmer, Spectrum 100 instrument. The absorption spectrum was recorded in the 4000-380 cm^{-1} region at a resolution of 4 cm^{-1}. Thermogravimetric analysis was performed on a Perkin Elmer apparatus (Pyris Diamond TG/DTA). The powders were heated to 1200 °C at a constant heating rate of 10 °C/min. The morphology of the powders was investigated by FESEM on a Jeol JSM-6700F instrument, operated at an acceleration voltage of 10 keV. Prior to investigation, samples were mounted on an aluminium stub with the help of carbon tape and sputter-coated with gold at a 60 mA deposition current. The morphology of the product was observed on a FEI Tecnai T20 transmission electron microscope (200 kV FEG high resolution TEM with LaB_6 electron source).

Results and Discussion

Formation of the white gel started 5–6 h after the reflux process of the reaction mixture. The reaction of calcium–zinc hydroxyapatite can be expressed as:

$$6(NH_4)_2HPO_4 + 8(NH_4)OH + (10-x)Ca(NO_3)_2 + xZn(NO_3)_2 \longrightarrow 20NH_4NO_3 + 6H_2O + Ca_{(10-x)}Zn_x(PO_4)_6(OH)_2 \quad ...(1)$$

Figure 1 shows the XRD patterns of BCP powders with varying Zn concentrations, calcined at 700 °C, 800 °C and 900 °C. The figure presents peaks due to hydroxyapatite (HA, ICCD card no. 09-432) as the main phase and *β*-tricalcium phosphate (*β*-TCP, ICCD card no. 09-169) as the secondary phase. However, a new phase parascholzite [$CaZn_2(PO_4).2H_2O$] (JCPDS 35-0495) starts to appear at 15 mol% zinc. The sharp and clear peaks confirmed the phase purity and crystallinity degree of the obtained powder. It can be seen from Fig. 1 that the relative intensity of the peaks reflecting the crystallinity level decreased as the amount of the dopant (Zn) increased. The present results are in a good agreement with earlier findings[13,20,21]. Change in crystallinity can be attributed to the fact that ionic radius of Zn^{2+} is less than that of Ca^{2+} (0.074 nm for $Zn^{2+}$and 0.099 nm for Ca^{2+}). The zinc ion distorts the crystal structure of HA and creates a structural mismatch, thus preventing further HA crystal growth[22]. This change in structure causes a change in the crystallinity.

The peaks of *β*-TCP phase increase with the increasing Zn concentration (Fig. 1b & 1c); the 15 mol% Zn-BCP sample show the highest intensity

of β-TCP peak at 2θ of 31.32°. The findings indicate that the amount of Zn incorporated in HA lattice influences the thermal stability of HA as it decreases with an increase in Zn fraction[15]. Further, the intensity of β-TCP peaks at 2θ = 28.10°, 29.96°, 31.32°, 34.5° and 36.69° becomes more intense and narrower for 15 mol% Zn-BCP, indicating the transformation of Zn-HA to Zn-substituted TCP beyond 10 mol% of zinc. A new phase, parascholzite, appeared in addition to the low-crystallinity apatite phase in 15 mol% rather than 18 mol% as reported by Miyaji *et al.*[14]

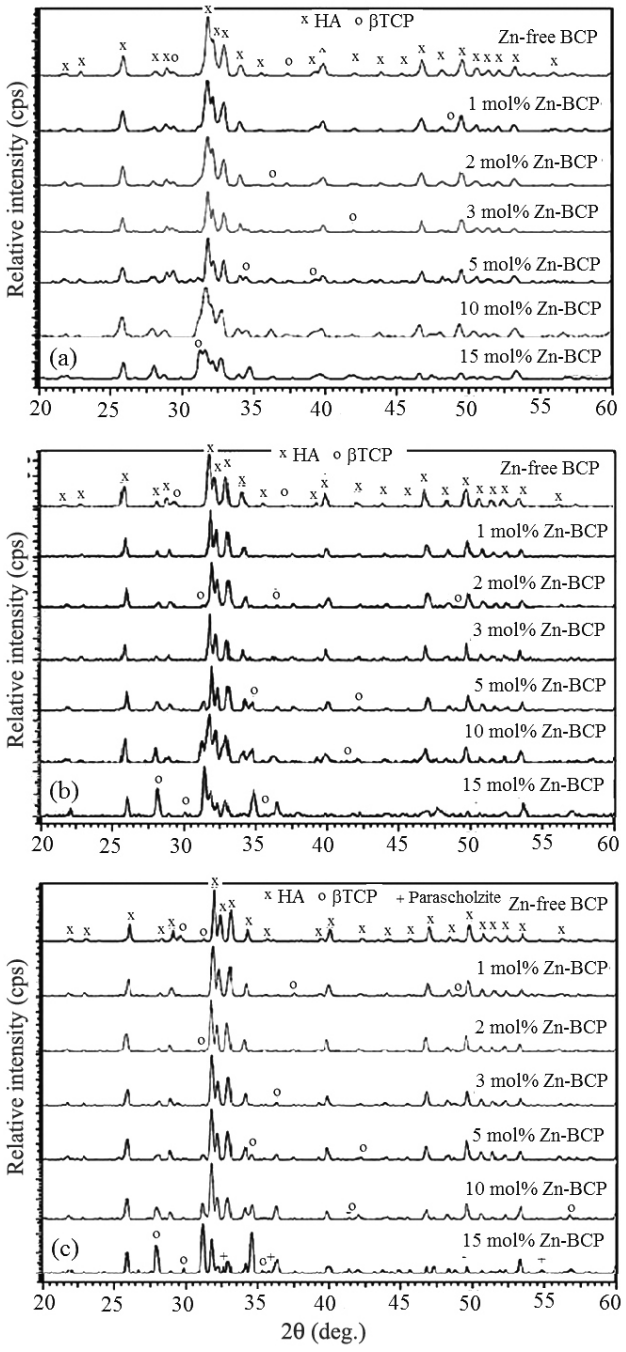

Fig. 1 – XRD patterns of various Zn-doped BCP powders at varying calcination temperature. [(a) 700 °; (b) 800 ℃; (c) 900 ℃].

XRD pattern of 10 mol% Zn-doped BCP powders calcined at different temperatures (500–900 °C) is presented in Fig. 2. The XRD pattern at 500 °C shows a poorly crystalline apatite. The transformation from the amorphous phase to crystalline phase takes place in a temperature range of 600–700 °C. The appearance of β-TCP starts in the powders calcined at 700 and 800 °C. The β-TCP peaks at 2θ = 28.10°, 31.32°, 34.5° and 36.69° increase in intensity and becomes narrower beyond 700 °C calcination temperature, indicating an increase in the amount of β-calcium phosphate phase. This is also indicative of the increased crystallinity[23].

The degree of crystallinity, X_c (= $\Sigma A_C/(\Sigma A_C = \Sigma A_{A,}$ where ΣA_C is the total area under crystal peaks and ΣA_A is the total area under amorphous peaks), was found to be 62.2% for Zn-free BCP sample which gradually decreases to 51.7% for 15 mol% Zn-BCP. The degree of crystallization of the samples gradually drops with a rise in the Zn content. This result is in the agreement with XRD analysis as discussed above and previous results that showed the crystallization degree for all the samples decreased with the increasing content of the Zn dopant[4,15].

Crystal size was estimated from the XRD pattern using Scherer's formula, $D_{(hkl)} = k\lambda/ (B_{1/2}\cos\theta)$ (where $D_{(hkl)}$ is the crystallite size (nm), k is the shape coefficient, 0.9, λ is the wavelength (nm) and $B_{1/2}$ is the full width at half maximum (FWHM) of X-ray reflection in radians). The FWHM values at (300) (2θ = 32.9°) was used to calculate the crystal size along with the a crystallographic axis. The results in Table 1 show that the crystal size of a-axis decreased with increased Zn content. The results from particle size

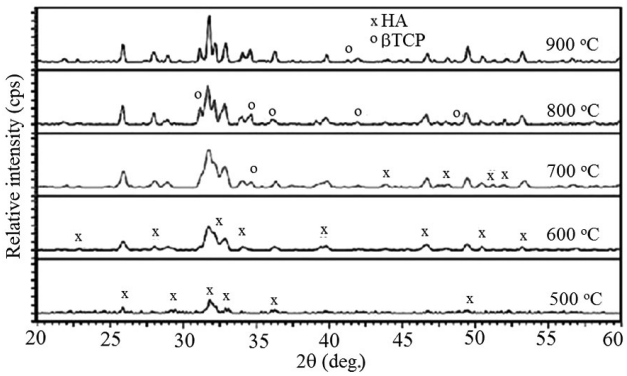

Fig. 2 – XRD patterns of 10 mol% Zn-BCP calcined at different temperatures.

analyser also depict the same trend. This finding is in a good agreement with the result as reported elsewhere[20].

The Rietveld refinement method provides evidence on the change in the lattice parameters (*a* and *c*) with Zn incorporation. The Rietveld refinement was extracted from XRD patterns of the synthesized powders (Supplementary Data, Fig. S1). The lattice parameters, *a* and *c*, of apatite consistently decreased with Zn substitution up to 10 mol% (Table 2). The observed decrease in the lattice parameters, *a* and *c*, is consistent with previous observations[15]. The decrease in the lattice parameters with Zn substitution is because of the ionic radius of Zn^{2+} is smaller than that of Ca^{2+}, and is also evident of Zn ion on inhibiting crystal growth of HA as discussed *vide infra* under XRD results.

FTIR spectra of Zn-doped BCP calcined at 700, 800, and 900 °C show vibrations characteristic of apatite phase (Supplementary Data, Fig. S2). The characteristic phosphate (mode υ_4) vibrations of HA are spotted at 563 and 600 cm^{-1} and the other modes υ_1 and υ_3 of PO_4^{3-} at 961, 1024 and 1085 cm^{-1} respectively [24,25]. The bands at 3500–3600 cm^{-1} and 630 cm^{-1} may be attributed to the presence of hydroxyl group (OH^-). Furthermore, the bands at 1380–1550 cm^{-1} correspond to CO_3^{2-} groups while those of 1420 and 875 cm^{-1} to HPO_4^{2-}. With increase in Zn, the separation of three PO_4^{3-} stretching peaks (961, 1024 and 1085 cm^{-1}) become obscure, and OH^- bending peak at 630 cm^{-1} broadens (Fig. S2). This is due to decreased crystallinity at higher Zn percentage[14]. This result is in good agreement with the results obtained from XRD, which confirm a decrease in crystallinity with an increase in zinc content. It is evident that the presence of zinc led to broadening of IR absorption bands characteristic of the PO_4^{3-} group and a decrease in the areas of OH^- absorption bands at 630 cm^{-1} (ref. 22). In the crystal structure of HA, the distance between O(H)–O (0.3068 nm) is less than OH^-– OH^- distance (0.344 nm), thus creating hydrogen bond between OH^- and PO_4^{3-} is easier than hydrogen bonding between two OH^- ions[15]. Hence, it may be deduced that the stretching vibration modes of OH^- are lower, which was caused by the hydrogen bonding created by oxygen between OH^- and PO_4^{3-}.

The FTIR spectra of 5 mol% Zn-BCP calcined at various temperatures is shown in Fig. 3. It can be seen that the PO_4^{3-} band of TCP at 1085 cm^{-1}, becomes narrower and sharper as the temperature increased, indicating the increase in the TCP composition in the powder. The effect of increased temperature on the HPO_4^{2-} peak is also be observed which becomes obscure and is compensated by a more intense hydroxyl (OH^-) peak at 630 cm^{-1}. A significant change in OH^- band intensity is observed as the temperature increased from 700 to 900 °C. This may

Table 1 — Single crystal size of Zn-doped BCP

Sample	Size of crystal grain *a*-axis(nm)	Particle size analyzer (nm)
Zn free BCP	46.1	198
1 mol% Zn-BCP	42.0	185
2 mol% Zn-BCP	40.5	159
3 mol% Zn-BCP	41.5	137
5 mol% Zn-BCP	39.9	149
10 mol% Zn-BCP	34.2	143

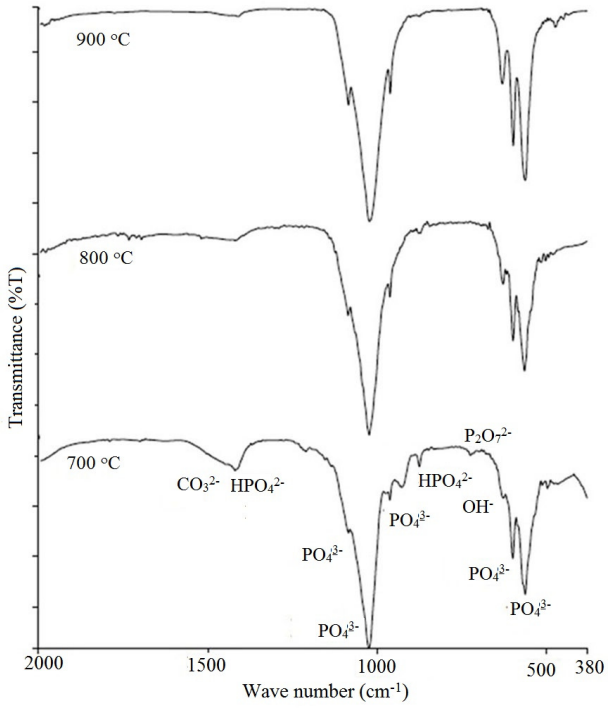

Fig. 3 – FTIR spectra of 5 mol% Zn-BCP calcined at 700 °C, 800 °C and 900 °C.

Table 2 — Unit cell parameters of HA, R_p (residual pattern) and χ^2 derived from Rietveld refinement

Sample	*a* (nm)	*b* (nm)	*c* (nm)	*V* (nm^3)	R_p	χ^2
Zn free BCP	$9.4129\pm3x10^{-4}$	$9.4129\pm3x10^{-4}$	$6.8766\pm4x10^{-4}$	843.01	0.178	1.82
2 mol% Zn-BCP	$9.4024\pm6x10^{-4}$	$9.4024\pm6x10^{-4}$	$6.8618\pm9x10^{-4}$	832.15	0.279	1.91
5 mol% Zn-BCP	$9.3982\pm5x10^{-4}$	$9.3982\pm5x10^{-4}$	$6.8584\pm7x10^{-4}$	831.40	0.297	1.89
10 mol% Zn-BCP	$9.3665\pm3x10^{-4}$	$9.3665\pm3\ x\ 10^{-4}$	$6.8422\pm3x10^{-4}$	825.81	0.152	1.78

be due to the increase in HA phase crystallinity at higher calcination temperatures. The stronger vibrational mode of OH^- indicates higher crystallinity of the powder. Moreover, the intensity of PO_4^{3-} band also increases with temperature and a decrease in intensity of CO_3^{2-} band at 1600 cm^{-1} is observed with a simultaneous increase in intensity of OH^- and PO_4^{3-}bands. These peaks indicate that the formation of the Zn-doped BCP phase involves the substitution of the carbonate for hydroxyl (A-type) and phosphate (B-type) groups. The larger number of peaks observed in the band of β-TCP with respect to HA probably arises from the three non-equivalent PO_4^{3-} tetrahedral in the crystal structure of β-TCP.

The TGA plot of 1 mol% Zn-BCP and 10 mol% Zn-BCP black gels shows clearly weight loss between 700–800 °C (Fig. 4). This type of loss is characteristic of calcium-deficient apatite (CDA). It is also confirmed by XRD results (Fig. 2), which show an increase in β-TCP peaks beyond 700 °C. The dissociation reactions of CDA powders ($1.50 \leq$ Ca/P $\leq$ 1.667) into HA and β-TCP occurs according to the following reactions[26]:

For temperature between 250 and 720 °C,

$$2HPO_4^{2-} \rightarrow P_2O_7^{4-} + H_2O,$$

and

for temperature between 750 and 900 °C,

$$P_2O_7^{4-} + 2OH^- \rightarrow 2PO_4^{3-} + H_2O$$

Figure 3 shows that the bands of HPO_4^{2-} groups at 880 cm^{-1} and $P_2O_7^{4-}$ groups at 715 cm^{-1} have high intensity at 700 °C. This band is derived from the condensation of the HPO_4^{2-} group to yield $P_2O_7^{4-}$, which at higher temperatures reacts further with HA to yield $Ca_3(PO_4)_2$. This is verified by the HPO_4^{2-} band at 875 cm^{-1} which shows a decrease in intensity and also by the absence of $P_2O_7^{4-}$ band at 715 cm^{-1} at higher temperatures. This confirms that decomposition of HPO_4^{2-} and $P_2O_7^{4-}$ into biphasic phase[18] takes place at temperatures beyond 700 °C.

The morphology of Zn-doped BCP nanopowders of various Zn concentrations calcined at 900°C is shown in Fig. 5. It is evident that individual particles

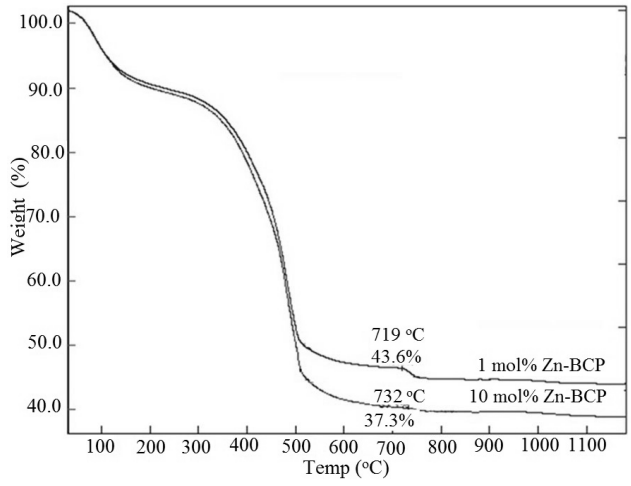

Fig. 4 – TGA curves of BCP powder doped with 1 mol% and 10 mol% Zn.

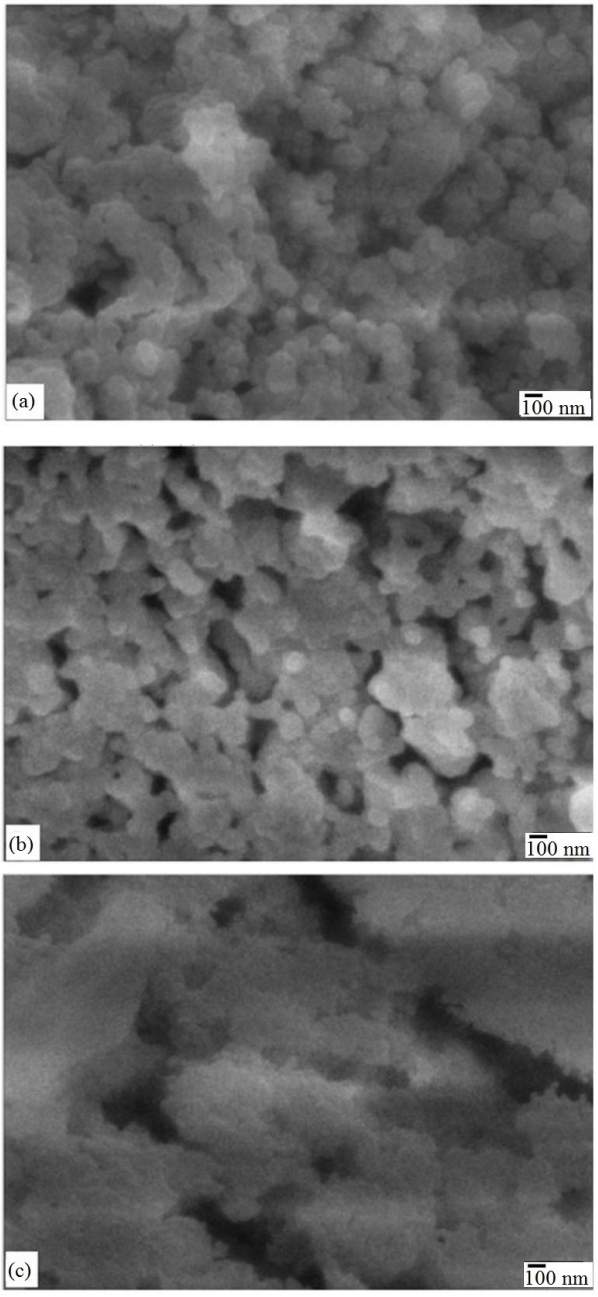

Fig.. 5 – FESEM micrograph of Zn-doped BCP powders calcined at 900 °C. [(a) 2 mol% Zn-BCP; (b) 5 mol% Zn-BCP; (c) 10 mol% Zn-BCP].

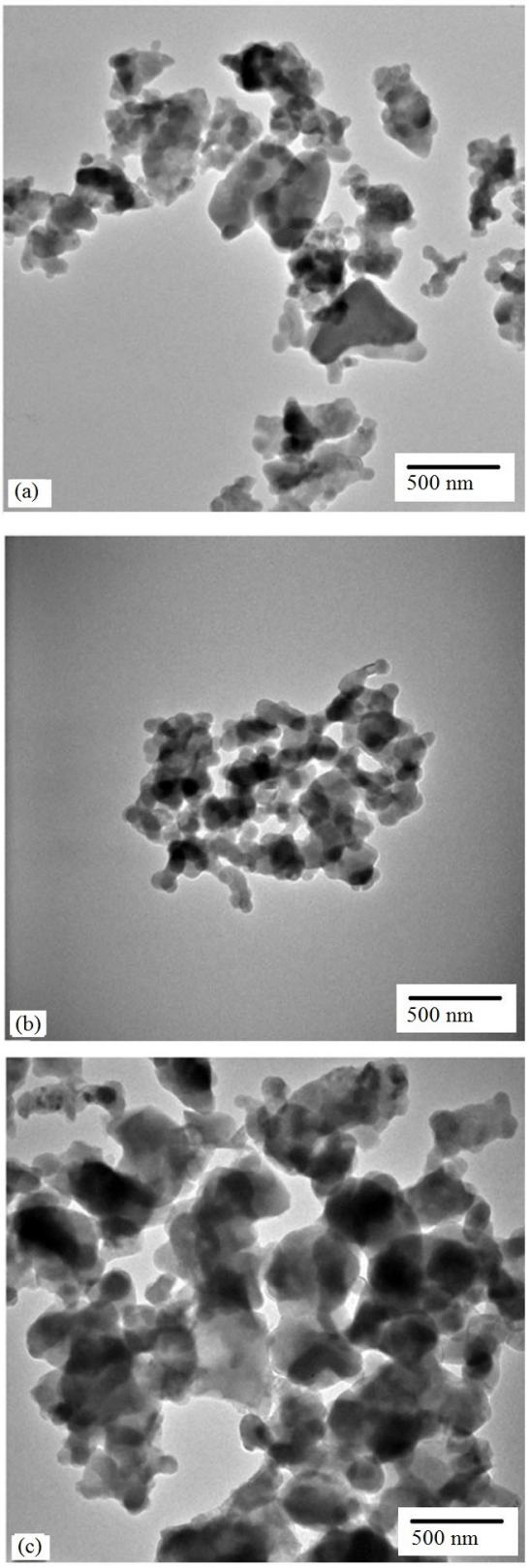

Fig. 6 – TEM micrograph of Zn-doped BCP powders calcined at 900 ºC. [(a) Zn free BCP; (b) 5 mol% Zn-BCP; (c) 10 mol% Zn-BCP].

of Zn-doped BCP are globular in shape. The powders show the agglomeration of the fine particles into sub-micro and microscale aggregates. The size of the agglomerates tends to increase as the amount of dopant increases. The micrograph of 10 mol% Zn-BCP shows a flat structure, resulting from the fusion of the spherical-particle aggregates. The fusion of the aggregates was observed to start at 5 mol% Zn-BCP, which increased with an increase in the dopant concentration.

The TEM image of BCP Zn free powders presented in Fig. 6a. It is evident of formation of nanocrystalline powder. Definite agglomeration of Zn-free BCP particles is observed. TEM morphology of 5 and 10 mol% zinc is shown in Fig. 6b and 6c. TEM micrographs show that the morphology of Zn-doped BCP depends on the amount of zinc. Agglomeration of the particles increases with an increase in Zn concentration. The incorporation of zinc in BCP causes a decrease in crystallinity as discussed in XRD results.

Conclusions

Zn-doped BCP nanopowders have been successfully synthesized via sol-gel technique. The influence of Zn concentration and calcination temperature on its phase behavior was studied. XRD results of the obtained Zn-doped BCP powders confirmed the formation of HA and β-TCP as the main and secondary phases respectively. Further, formation of the parascholzite as the third phase took place in the 15 mol% Zn-BCP and not in 18 mol% Zn-BCP as reported earlier[14]. The crystallinity of the samples decreased with an increase in Zn content due to the fact that ionic radius of Zn^{2+} is less than Ca^{2+}. Zinc ion distorts HA and creates a structural mismatch, thus preventing further HA crystal growth. This finding is in accordance with Rietveld refinement showed that the lattice parameters, *a* and *c*, of the apatite structures decreased as Zn substitution increased. FTIR analysis of the calcined powders revealed a decrease in crystallinity with higher zinc content, while PO_4^{3-} of TCP at 1085 cm^{-1} becomes narrower and sharper at higher temperatures. The morphology of the samples showed that dopant concentration changes the morphology of Zn-doped BCP particles. The present study shows that an increase in Zn doping of BCP affected the phase composition, crystallization and microstructure of the samples.

Supplementary Data

Supplementary data associated with this article, viz., Figs S1 and S2, are available in the electronic form at http://www.niscair.res.in/jinfo/ijca/IJCA_53A(02)152-158_SupplData.pdf.

Acknowledgement

The authors thank Ministry of Higher Education (MOHE) Malaysia, for the financial support through the FRGS scheme (Project no. FRGS11-025-0173).

References

1 Legeros R Z, Lin S, Rohanizadeh R, Mijares D & Legeros J P, *J Mater Sci: Mater Med*, 14 (2003) 201.
2 Daculsi G, Laboux O, Malard O & Weiss P, *J Mater Sci: Mater Med*, 14 (2003) 195.
3 Li B, Liao X, Zheng L, Zhu X, Wang Z, Fan H & Zhang X, *Acta Biomater*, 8 (2012) 3794.
4 Kaygili O & Tatar C, *J Sol-Gel Sci Technol*, 61 (2011) 296.
5 Garrido C A, Lobo S E, Turibio F M & Legeros R Z, *Int J Biomater*, 2011 (2011) 1.
6 Ito A, Otsuka M, Kawamura H, Ikeuchi M, Ohgushi H, Sogo Y & Ichinose N, *Curr Appl Phys*, 5 (2005) 402.
7 Renaudin G, Jallot E & Nedelec J M, *J Sol-Gel Sci Technol*, 51 (2008) 287.
8 Shepherd J H, Shepherd D V & Best S M, *J Mater Sci: Mater Med*, 23 (2012) 2335.
9 Adzila S, Sopyan I, Singh S, Pusparini E & Hamdi M, *Indian J Chem*, 52A (2013) 739.
10 Wang X, Ito A, Sogo Y, Li X & Oyane A, *Acta Biomater*, 6 (2010) 962.
11 Yamaguchi M, *Mol Cell Biochem*, 338 (2010) 241.
12 Yamaguchi M, *Mol Cell Biochem*, 366 (2012) 201.
13 Devanand V G, Ramasamy S, Ramakrishnan V & Kumar J, *3 Biotech*, 1 (2011) 173.
14 Miyaji F, Kono Y & Suyama Y, *Mater Res Bull*, 40 (2005) 209.
15 Li M, Xiao X, Liu R, Chen C & Huang L, *J Mater Sci: Mater Med*, 19 (2008) 797.
16 Bezzi G, Celotti G, Landi E, La Torretta T M G, Sopyan I & Tampieri A, *Mater Chem Phys*, 78 (2003) 816.
17 Nawawi N A, Sopyan I, Ramesh S & Afzeri, *Asia-Pac J Chem Eng*, 6 (2011) 823.
18 Sopyan I & Rahim T A, *Mater Manuf Process*, 27 (2012) 702.
19 Larson A C & Dreele R B V. *General Structure Analysis System (GSAS)*, (Los Alamos National Laboratory Report LAUR 86-748) 2004
20 Ren F, Xin R, Ge X & Leng Y, *Acta Biomater*, 5 (2009) 3141.
21 Tank K P, Sharma P, Kanchan D K & Joshi M J, *Cryst Res Technol*, 46 (2011) 1309.
22 Bigi A, Foresti E, Gandolfi M, Gazzano M & Roveri N, *J Inorg Biochem*, 58 (1995) 49.
23 Sanosh K P, Chu M C, Balakrishnan A, Kim T N & Cho S J, *Bull Mater Sci*, 32 (2009) 465.
24 Sopyan I & Natasha A N, *Ionics*, 15 (2009) 735.
25 Panda R N, Hsieh M F, Chung R J & Chin T S, *J Phys Chem Solids*, 64 (2003) 193.
26 Lazić S, Zec S, Miljević N & Milonjić S, *Thermochim Acta*, 374 (2001) 13.